Acta Geotechnica (2006) 1:195–209
DOI 10.1007/s11440-006-0018-4

RESEARCH PAPER

# Calculating the effective permeability of sandstone with multiscale lattice Boltzmann/finite element simulations

**Joshua A. White · Ronaldo I. Borja · Joanne T. Fredrich**

Received: 1 September 2006 / Accepted: 10 October 2006 / Published online: 18 November 2006

**Abstract** The lattice Boltzmann (LB) method is an efficient technique for simulating fluid flow through individual pores of complex porous media. The ease with which the LB method handles complex boundary conditions, combined with the algorithm's inherent parallelism, makes it an elegant approach to solving flow problems at the sub-continuum scale. However, the realities of current computational resources can limit the size and resolution of these simulations. A major research focus is developing methodologies for upscaling microscale techniques for use in macroscale problems of engineering interest. In this paper, we propose a hybrid, multiscale framework for simulating diffusion through porous media. We use the finite element (FE) method to solve the continuum boundary-value problem at the macroscale. Each finite element is treated as a sub-cell and assigned permeabilities calculated from subcontinuum simulations using the LB method. This framework allows us to efficiently find a macroscale solution while still maintaining information about microscale heterogeneities. As input to these simulations, we use synchrotron-computed 3D microtomographic images of a sandstone, with sample resolution of 3.34 μm. We discuss the predictive ability of these simulations, as well as implementation issues. We also quantify the lower limit of the continuum (Darcy) scale, as well as identify the optimal representative elementary volume for the hybrid LB–FE simulations.

**Keywords** Finite elements · Lattice Boltzmann · Multiscale simulation · Porous media · Synchrotron microtomography · Upscaling

## 1 Introduction

Quantifying the permeability of geomaterials poses a challenging task to the mathematical modeler because this parameter depends strongly on the extremely heterogeneous and complex microstructure of such materials [5, 13–16, 18, 21, 22, 30, 31]. In addition to porosity, the effective permeability of geomaterials depends on pore geometry and connectivity, tortuosity of flow, the presence of stagnant pockets created, for example, by dead-end pores, and the degree of saturation [5]. Microstructural changes induced by compaction or dilation banding could alter the effective overall permeability of the medium by several orders of magnitude [3, 4, 26, 27]. The presence of fissures in a porous rock can induce preferential flow directions, so that when viewed as a continuum the flow properties could exhibit strong anisotropy [26, 27]. Unless we resort to statistical simulations (see e.g., [1]), limitations of continuum mechanics descriptions that have been the cornerstone of many flow models inhibit our ability to incorporate all of these microscale factors in quantifying the effective permeability of geomaterials.

---

J. A. White · R. I. Borja (✉)
Department of Civil and Environmental Engineering,
Stanford University, Stanford, CA 94305, USA
e-mail: borja@stanford.edu

J. T. Fredrich
Sandia National Laboratories,
Albuquerque, NM 87185-0751, USA

*Present Address:*
J. T. Fredrich
Exploration and Production Technology Group,
BP America, Inc., Houston, TX 77079, USA

Recent advances in high resolution 3D imaging offer unparalleled opportunities for predicting macroscopic properties of earth materials from microstructural measurements [2, 4, 14, 15, 24, 29]. High-resolution 3D synchrotron computed microtomographic experiments provide micron-scale image resolution that is superior to conventional X-ray computed tomography (CT). The trade-off is that samples are correspondingly small, approaching millimeters in diametric dimensions for optimal image resolution. However, despite the minute size of the specimen the technology provides significant information on the microscopic structure of complex porous media.

The past decade has also seen remarkable progress in the numerical modeling of fluid flow processes at the pore scale. One of the most promising techniques is the lattice Boltzmann (LB) method [6, 13, 14, 16–20, 23, 30, 32]. The LB approach considers a typical volume element of fluid as composed of a collection of particles that are represented in terms of a velocity distribution function at each point in space. The LB method utilizes nearest neighbor information, so it is ideally suited for massively parallel computers. The approach provides insight into the internal velocity and kinetic energy distributions at the pore scale, and can detect preferential flow paths and channeling phenomenon not possible with any available continuum flow models. Direct LB simulation on micron-scale 3D image data thus offers a significant potential for new fundamental insights and understanding of fluid flow processes in a material with a complex microstructure.

There are, however, potential concerns in any direct numerical simulation, whether it be fluid flow, wave propagation, electric transport, or others. In the first place, such calculations are time-consuming and extremely memory intensive. For example, a typical LB sparse storage scheme requires about 100 bytes/fluid-cell. Therefore, a 3D volume at 30% porosity and modeled with $1000^3$ cells would require 30 Gb of memory to store the relevant information throughout the simulation. This storage space is well beyond the capability of a typical workstation. Secondly, macroscopic properties are often measured by averaging microscopic quantities over the domain. In many cases, however, one is not only interested in a single global value, but also in the spatial variation of the continuum quantity. For example, in the region of a deformation band there could be pervasive heterogeneity in the permeability field, even in a very ‘‘small’’ specimen [3, 4, 7]. A simple global averaging approach masks the complexity of these spatial variations by smearing them through the specimen.

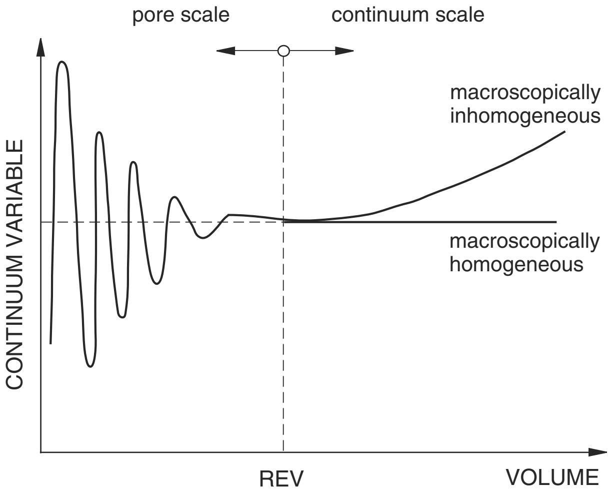

**Fig. 1** Definition of pore and continuum scales, as well as REV. Figure partially reproduced from [5]

In a discussion of such spatial variations, it is helpful to introduce the notion of a representative elementary volume (REV). The REV has been accepted in principle for quite some time now and is depicted pictorially in Fig. 1. Here, the horizontal axis represents the volume of an element whereas the vertical axis denotes any continuum variable such as porosity or mass density of this element. The centroid of the element is the ‘‘material point’’ whose continuum properties are represented by those of the material inside the volume. For large volumes the continuum variable may undergo gradual changes as the volume is reduced, especially when the domain considered is macroscopically inhomogeneous. Below a certain value of the volume, however, large fluctuations in the values of the continuum variable may be expected as the dimensions of the volume approach those of a single pore. This transition point defines the boundary between continuum and pore scales. If we are interested in spatial variations in some continuum variable, this transition point represents the target scale at which we wish to measure the fluctuations. If our volume elements are too large we can no longer resolve small fluctuations, but if they are too small we violate the continuity assumption.

With this background in hand we now state the objectives of this paper, which are twofold. First, we want to quantify the REV for a geomaterial, specifically a sandstone, based on measured micron-scale 3D images and calculated kinetic energies generated by direct LB simulations on these images. Second, we want to combine the LB technique with the finite element (FE) method for solving the pore scale hydrodynamics in a given flow domain. The FE method is the most widely used continuum model for the numerical analysis of complex boundary-value problems, and its marriage with the LB technique offers unique opportunities for attacking the pore scale problem in a truly multiscale way. The proposed hybrid modeling technique delivers at least two potential benefits. First, because the domain of the LB simulations is reduced to the smallest REV scale, LB calculations now become significantly cheaper and less memory intensive (the cost of the FE calculations is almost nil compared to the cost of the LB simulations). Second, inhomogeneities of the macroscale variables such as the effective permeability can now be quantified in the flow domain. These benefits can be realized more clearly in 3D simulations as we shall demonstrate with Castlegate sandstone.

## 2 Description of LB–FE model

The challenging aspect of flow in porous media is that the governing equations shift as one moves from one length scale to the next. At the macroscale, we are interested in solving the diffusion equation in the domain of interest, subject to specified boundary conditions. We can readily solve this problem using a variety of continuum methods (e.g., FE), but first we must have some idea of the permeability of the porous medium. This permeability, however, is an averaged representation of complex solid–fluid interactions occurring at a smaller scale. Typical continuum methods have no way of probing the pore scale to determine the required permeability field. As a result, we typically turn to experimental data or simple analytical relations.

As we look one level down, the flow through individual pores is governed by the Navier–Stokes equations, whose solution we may recover using LB. In principle, we could just use a very large LB simulation to obtain the macroscopic solution we wanted in the first place, but we are limited by the realities of current computational resources. Beyond a certain volume, it becomes impractical to discretize every pore with sufficient fidelity and solve for the complete flow field.

The question we attempt to address in this work is whether we can apply a multiscale approach to sidestep the inherent difficulties of the single-scale methods just described. We instead propose a hybrid method that combines the advantages of both LB and FE methods. In the macroscopic domain, we solve the diffusion equation on a FE mesh. Instead of using experimental data to calibrate the permeability field, we perform a small LB simulation within each element to examine the microstructure and assign an appropriate permeability tensor. Thus we are able to incorporate information about microscale interactions into our continuum picture. Simultaneously, we limit the computational requirements by running the expensive LB simulations in a series of small domains instead of one large one. In this way, we approach the solution from a perspective which is appropriate to the multiscale nature of the problem. Our goal in the next few sections is to establish the details of this framework.

We would like to emphasize, however, that the proposed framework is by no means a replacement for detailed LB simulations. We have approached the problem from a continuum perspective, in which we are interested in the macroscopic effects of microscale behavior. Our simulations, however, do not resolve the details of the flow field in every pore. In many cases, these details might be the primary objective of the simulation—perhaps in an investigation of trapping phenomena or mixing behavior. As such, a detailed LB simulation may be appropriate and necessary. Our perspective in this paper, however, is that the LB method is a powerful microscale technique, but scales poorly when one is interested in field-scale solutions.

### 2.1 Lattice Boltzmann technique

The lattice Boltzmann technique is uniquely suited to modeling the complexities of fluid flow through disordered media, including flow through porous geomaterials [2, 13, 14, 16, 18, 19, 21]. Given the ease with which the method handles complex internal boundaries, LB is a natural choice for our microscale simulations. In the following, we provide a brief description for the unfamiliar reader. Several excellent references that review the development and details of the LB method may be found in the literature, including [10, 28].

In LB, we do not solve the Navier–Stokes (NS) equations directly, but rather a discretization of the Boltzmann equation is formulated such that the velocity and pressure fields satisfy the NS equations. In our computations the two-phase microstructure of the porous medium is represented as a bitmap image, in which each pixel (in 2D) or voxel (in 3D) represents either solid or void. Each void pixel is assigned a node, and the pore-space is represented by a lattice connecting each of these nodes. A typical unit cell for the lattice is illustrated in the appendix. The unknown quantities at each node are not velocity and pressure, but rather a discrete distribution function $f_i(\boldsymbol{x},t)$. This function represents the probability of finding a particle at location $\boldsymbol{x}$ and time $t$ moving with a certain discrete velocity $\boldsymbol{e}_i$. These discrete velocities point along the inter-node links in the lattice. The particle distribution satisfies the discrete-velocity Boltzmann equation,

$$\frac{\partial f_i}{\partial t} + \boldsymbol{e}_i \cdot \nabla f_i = \Omega_i, \tag{1}$$

where $\Omega_i$ is a collision term that accounts for the net addition of particles moving with velocity $\boldsymbol{e}_i$ due to inter-particle collisions. Once we solve for the particle distribution function, quantities such as density, pressure, and velocity may be recovered from the first two moments of these distributions. In our implementation we solve a discretized version of Eq. 1 using the linearized Bhatnagar, Gross, and Krook (LBGK) scheme [6] on D2Q9 and D3Q19 lattices [23]. Internal solid-fluid boundaries have been handled using the popular "bounce-back" rule. It should be noted that much recent work has focused on improved hydrodynamic boundary conditions [17, 20, 32], accelerating convergence [30], and on other improvements to the standard methods. Our goal in this work is not to focus on these details, but rather outline a multiscale framework. Our methodology is by no means limited to the particular features chosen here.

In the hybrid LB–FE model, the global domain is divided into a series of rectilinear sub-cells, each of which will become a finite element. To determine the local permeability in each sub-cell, we are interested in solving for the steady-state flow field $\boldsymbol{v}(\boldsymbol{x})$ resulting from a hydraulic gradient $\nabla h$ applied along basis direction $\boldsymbol{e}_j$. For now, let us temporarily postpone the discussion of the imposed sub-cell boundary conditions. With the velocity field determined, we may recover the $j$th column of the element permeability tensor $\boldsymbol{k}$ according to

$$k_{ij} = -\langle v_i(\boldsymbol{x})\rangle \frac{\mu}{(\nabla h)_j}, \tag{2}$$

where $\mu$ is the kinematic viscosity, and $\langle ... \rangle$ denotes a volume average over the domain. One could also measure the specific discharge through a single plane to determine the permeability; both methods produce the same results. To determine the complete tensor, a separate simulation must be run along each basis direction $\boldsymbol{e}_j$—i.e., two in 2D and three in 3D.

We return now to the issue of boundary conditions for the sub-cell simulations. The primary assumption we have made in dividing the domain into individual sub-cells is that the element permeability can be approximated with no knowledge of neighbor cells—i.e., a locality assumption. We therefore need to impose boundary conditions that will reasonably mimic the flow situation in the complete porous medium. In this work, we have adopted periodic conditions in which the particle distributions leaving one side of the domain re-enter at the opposite plane. The element is therefore treated as a unit cell in an infinite domain. The hydraulic gradient is then imposed using a body force scheme by exploiting the fact that force is equal to change in momentum. During each time step, we add additional density to the forward-pointing particle distributions, while subtracting the same from the backward directions. This does not alter the total density at the node, but adds a constant amount of momentum in the positive direction.

By using a periodic scheme, however, we encounter the additional geometric restriction that the solid-void geometry on the outgoing face must match the geometry on the incoming face. This difficulty is readily overcome by simply mirroring the domain in all directions. If this is done explicitly, however, the lattice size grows by a factor of four in 2D, and eight in 3D. A scheme for side-stepping this difficulty and implicitly mirroring the domain, while still working on the original size lattice, has been presented in [14]. We have employed this scheme for our 3D simulations, with significant computational savings. In 2D the computational requirements were not stringent, and the simpler explicit scheme was used.

## 2.2 Finite element technique

Having solved for the local element tensors, we may assign the appropriate permeability at every Gauss point in the global finite element mesh. A straightforward solution of the diffusion equation, using a standard Galerkin formulation, yields the desired macroscopic pressure field. Compared with the LB simulations, the additional computational time required by the FE solution is negligible.

Our FE implementation contains one unusual feature, however. In the standard formulation of the diffusion equation, the permeability tensor is assumed symmetric. This then leads to a symmetric, positive definite stiffness matrix after assembly. In our sub-cell LB simulations, however, the measured permeability tensors are *not* symmetric, leading to an asymmetric stiffness matrix and requiring an appropriate linear solver [8]. In the numerical examples to follow, we explore the effect this asymmetry has on the solution by comparing results to cases when (a) the tensor has been symmetrized, and (b) the tensor has been assumed isotropic.

### 2.3 Boundary between micro- and Darcy scales

A crucial step for the hybrid framework is determining an appropriate FE discretization. By choosing a very coarse mesh, we are forced to do expensive LB simulations on each finite element (treated as a sub-cell) and lose a great deal of computational efficiency. By choosing a highly refined FE mesh, on the other hand, we could get into the range of the pore scale where continuum approximations clearly are inappropriate. The challenge, then, is to find a method to quantify this transition from pore scale to continuum scale behavior.

Returning to Fig. 1, we propose that the onset of the continuum scale be quantified by observing the fluctuations in the behavior of an energy measure—the local rate of mechanical dissipation:

$$\mathcal{D}(\boldsymbol{x}) = (2\mu)\epsilon_{ij}\epsilon_{ij}; \quad \epsilon_{ij} = \frac{1}{2}\left(v_{j,i} + v_{i,j}\right), \tag{3}$$

where $\epsilon_{ij}$ is the symmetric gradient of the velocity field. As pointed out by Pilotti et al. [22], energy dissipation governs the evolution of the total head, and thus is closely linked to the absolute permeability of the medium. As such, it can provide a meaningful indicator of the onset of the Darcy scale, unlike other macroscale variables such as porosity which are insufficient to describe the permeability of an arbitrary porous medium [5]. If we choose a REV such that the dissipation behaves as a continuum variable, one expects that any quantity that depends on it will also behave as a continuum variable.

In the next two sections, we present numerical results using the hybrid LB–FE framework we have established to clarify this discussion. We begin with three 2D examples with artificially generated porous media. We conclude with a 3D example based on microtomographic images of an actual sandstone.

## 3 Two-dimensional examples

Our first 2D example is a macroscopically homogeneous porous medium (Fig. 2). The binary pore/void image consists of $1800^2$ pixels (Fig. 2a). To obtain a reference solution, we performed a LB simulation in the entire domain. A constant pressure was assigned along the left and right boundaries, and a no flow condition was imposed on the other two edges. The question of how best to assign pressure boundary conditions in the LB technique has prompted several studies [17, 20, 32]. We have adopted an approach based on the work of Zou and He [32] for the D2Q9 lattice. In an appendix we present a formulation for the D3Q19 lattice. The assigned pressure drop was kept small enough for the flow to remain in the low Reynold's number regime and ensure Darcy's law remains valid. With boundary conditions established, the LB simulation was run until steady state was reached. Our criteria for convergence was based upon the rate of change of the velocity field, with a convergence tolerance of $10^{-7}$. This value was found sufficient to guarantee that the flow field had reached steady state. Figure 2b illustrates the resulting pressure field, an essentially linear head drop from inlet to outlet.

Having solved for the velocity field within the pore space, we can calculate the local rate of mechanical dissipation at each point using Eq. 3. In analogy to Fig. 1, we then averaged this property over increasingly large volumes (Fig. 3). In the figure, the volume is represented by its side length $s$, normalized by the full domain dimension $L$. For small element dimensions, we see dramatic fluctuations in the averaged property, indicative of the dominance of microscale behavior. As the volume is increased, however, these oscillations reduce dramatically and indicate the onset of what we would consider the macroscale. Figure 3 thus provides a meaningful way of determining how large an REV is necessary for the continuum assumption to be valid. We note, however, that the measured dissipation will also depend on where in the sample the averaging volume is located. Therefore, it makes sense to sample at several different points in the domain in order to obtain a more complete picture of the fluctuation behavior.

It should be noted that we are at an advantage in having a reference solution in a large domain in order to develop Fig. 3. In practice one would most likely take an incremental approach, beginning with some small dimension and running increasingly large LB simulations until confident that the continuum scale had been reached. In either case, observing the averaged behavior of the dissipation, or some other measure of interest, can provide a quantitative way to evaluate this scale transition.

Based on the previous discussion, we felt that an 18 × 18 discretization of the flow domain would yield sub-cells of sufficient size to be treated as REVs. Again, our discretization criteria is to choose sub-cells as small as possible to gain the greatest computational advantage, but not so small that we violate the necessary continuum assumption at the FE level. Nevertheless, it is not necessary to find an REV sufficiently large that *all* oscillations have disappeared. Rather, we are merely interested in avoiding the dramatic microscale oscillations. The finite element solution is then in

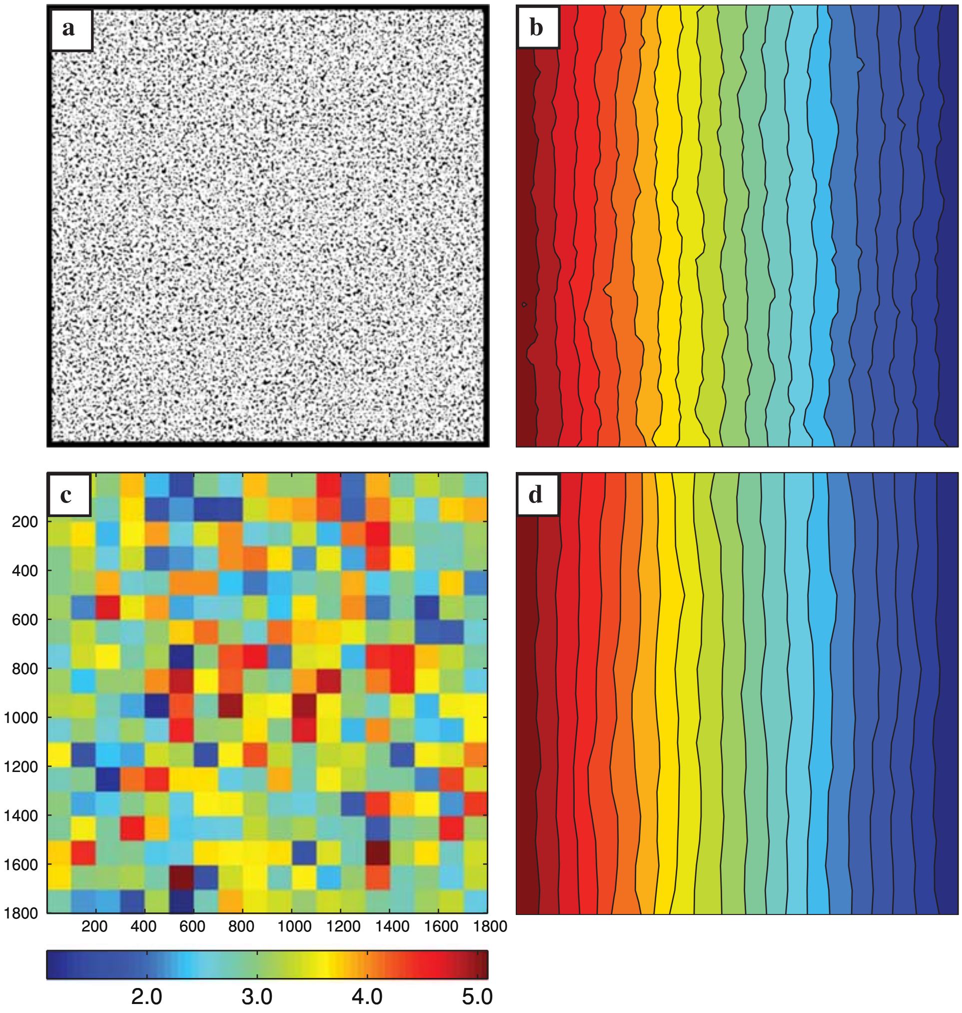

**Fig. 2** **a** Pore/void image of a homogeneous porous medium. **b** Pressure field from a LB simulation in the entire domain. **c** Permeability field ($k_{11}$ component) measured by sub-cell LB simulations, in units of (lattice unit)$^2$. **d** Predicted field from combined LB–FE approach

place to handle the remaining (Darcy scale) heterogeneity. At the conclusion of this section, we present a brief refinement study to address these issues in more detail.

Having determined an appropriate REV, the porous image was divided into 324 sub-domains. In each domain two LB simulations were run—with the hydraulic gradient applied along each basis direction—to determine the complete permeability tensor. In general, we have employed a convergence tolerance of $10^{-6}$ for all sub-cell computations, slightly lower than the tolerance used in the reference solution. Given that the sub-cell simulation provides only an approximation to the local permeability tensor, with inherent inaccuracies, we found an extremely high sub-cell tolerance does not translate into additional accuracy at the global level. Figure 2c illustrates the $k_{11}$ component of the permeability field estimated using this approach. It is interesting to note that, despite the medium's appearance of homogeneity, significant fluctuations are present in the element permeabilities.

Possessing the necessary permeability information, we represented the domain with an 18 × 18 FE mesh, in which each Gauss point was assigned the appropriate local tensor. A trivial amount of additional computation then yielded the global solution for the pressure field, Fig. 2d. We have applied boundary conditions on the LB–FE mesh consistent with the reference LB solution. One should recognize, however, that having determined the permeability field we may assign an arbitrary variety of boundary conditions on the mesh—perhaps examining flow in the perpendicular

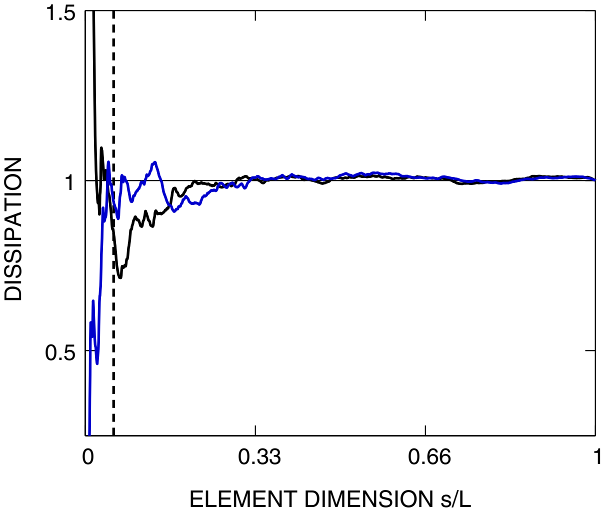

**Fig. 3** Mechanical dissipation rate averaged over increasingly large volumes at two different locations in the domain. Values have been normalized by the global average. The *dashed line* corresponds to an element dimension of 1/18

direction, or some source-to-sink behavior. In contrast, the invested computational work in the pure LB approach only yields a single solution.

As noted in the introduction, one of the major goals of this study is to examine continuum scale heterogeneity—for example, permeability in the presence of a compaction band (Fig. 4). For our next two examples, we have therefore introduced heterogeneity into the pore/void images. Figure 5 illustrates a low porosity inclusion surrounded by a highly permeable matrix, analogous to a compaction band which has formed a transport barrier for the fluid flow. Figure 6 illustrates the complimentary case, a high porosity band surrounded by a less permeable matrix. This example mimics a dilation band forming a high-porosity conduit. Note that in both images the band thickness is approximately equal. In reality, the thickness of a dilation band is typically smaller than that of a compaction band; in the dilation case, grains tend to separate and create opening fractures, and thus band width is limited [3, 9].

Our simulation approach is identical to the first example, using an 18 × 18 LB–FE discretization. The effects of the two bands are clearly visible in the measured permeability field, as well as in the resulting pressure solutions. In the LB–FE prediction, we lose some of the small scale oscillations in the iso-contours, but otherwise maintain an accurate description of the complexities of the pressure field.

Table 1 compares the effective (global) $k_{11}$ permeability for each sample as predicted by the pure LB and the combined LB–FE approach. In general, we have relied on the full, typically asymmetric $\boldsymbol{k}$ tensor in our simulations. We have also taken the opportunity to compare results when we have symmetrized the subcell tensors, and when we have adopted an isotropic assumption. In the case of the isotropic tensor the permeability coefficient is taken as the mean of $k_{11}$ and $k_{22}$. In these three examples, the underlying assumption about the tensor form has only minor effects on the solution, suggesting that the porous media we have generated are locally isotropic. In the case of the compaction example, however, the isotropy assumption introduced a significant error in the prediction. In the 3D example to follow, we will see that the form of the permeability tensor has a significant effect on accuracy in the case of a general porous medium.

Table 1 also presents comparisons of the computational requirements for each approach. We first note

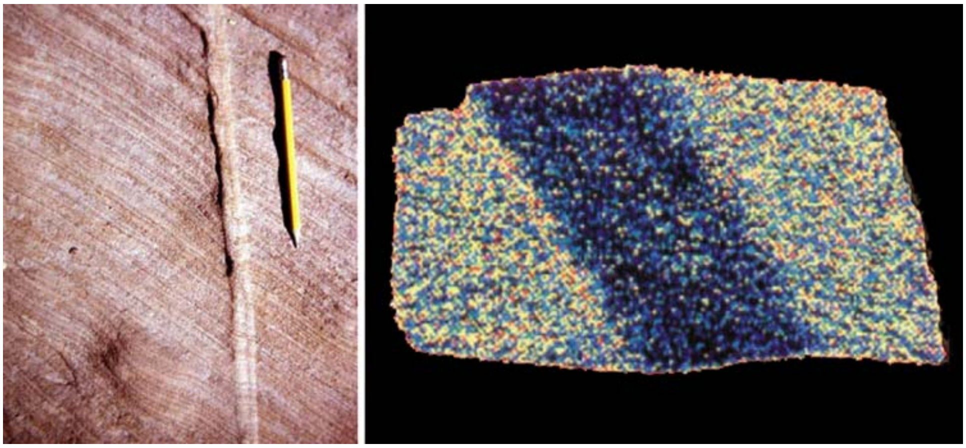

**Fig. 4** Photographs of a compaction band in Aztec sandstone (*left*) and cross section from a CT scan (*right*). The image is colored by the porosity distribution. The average porosity of the parent sandstone is about 20%, but only 5–7% within the band. Photographs reproduced from [3]

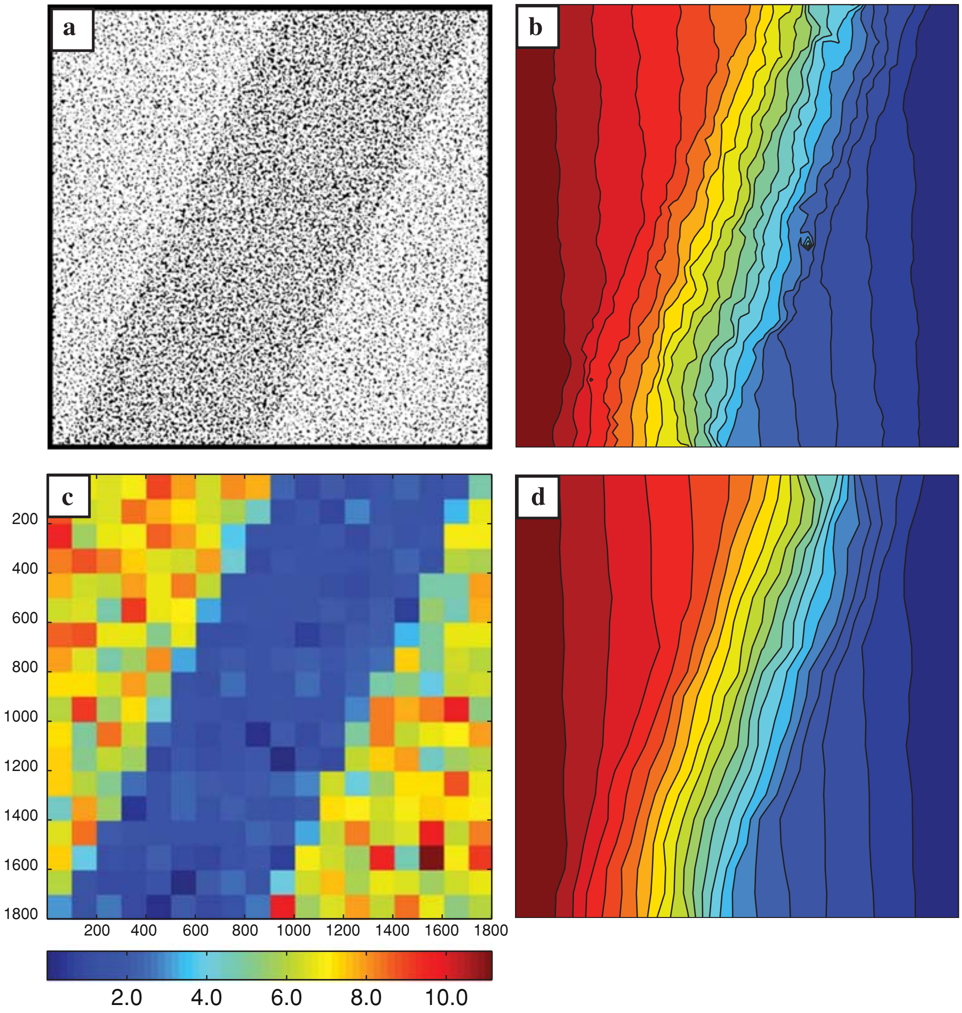

**Fig. 5** **a** Pore/void image of a compaction band analog. **b** Pressure field from a LB simulation in the entire domain. **c** Permeability field ($k_{11}$) measured by sub-cell LB simulations. **d** Predicted pressure field from combined LB–FE approach

**Table 1** Comparison of effective $k_{11}$ permeability values from the reference solution and using an 18 × 18 LB–FE discretization

| | l.u.$^2$ | Error (%) | Hours | Memory (Mb) |
|---|---|---|---|---|
| Homogeneous | | | | |
| Reference solution | 3.05 | | 1.1 | 134.0 |
| Full tensor | 3.05 | <0.01 | 1.4 | 1.7 |
| Symmetrized | 3.05 | <0.01 | 1.4 | 1.7 |
| Isotropic | 3.06 | <0.01 | 1.4 | 1.7 |
| Compaction band | | | | |
| Reference solution | 2.80 | | 8.4 | 136.0 |
| Full tensor | 2.82 | 0.7 | 3.0 | 1.7 |
| Symmetrized | 2.82 | 0.7 | 3.0 | 1.7 |
| Isotropic | 2.94 | 5.0 | 3.0 | 1.7 |
| Dilation band | | | | |
| Reference solution | 3.43 | | 4.6 | 133.0 |
| Full tensor | 3.44 | 0.3 | 2.6 | 1.6 |
| Symmetrized | 3.44 | 0.3 | 2.6 | 1.6 |
| Isotropic | 3.44 | 0.3 | 2.6 | 1.6 |

All simulations were run on identical 3.2 GHz processors

that LB is a memory intensive method, given that the particle distributions form an unusually large set of unknowns—9 in our 2D examples and 19 in our 3D example. In these 2D examples the memory requirements are not severe, but in 3D even modest size problems can quickly exceed the memory capacity of a typical workstation. In the LB–FE approach, we no longer require that the entire domain be stored in memory simultaneously, but rather only a small sub-cell. As a result, we notice that the memory requirement has been reduced by a factor of 1/81. If we had used an implicit mirroring scheme, this factor would be 1/324.

We also observe that the total required wall time compares favorably with the pure LB approach, despite having to run 2 × 324 separate sub-cell simulations. We offer a word of caution, however, in that a

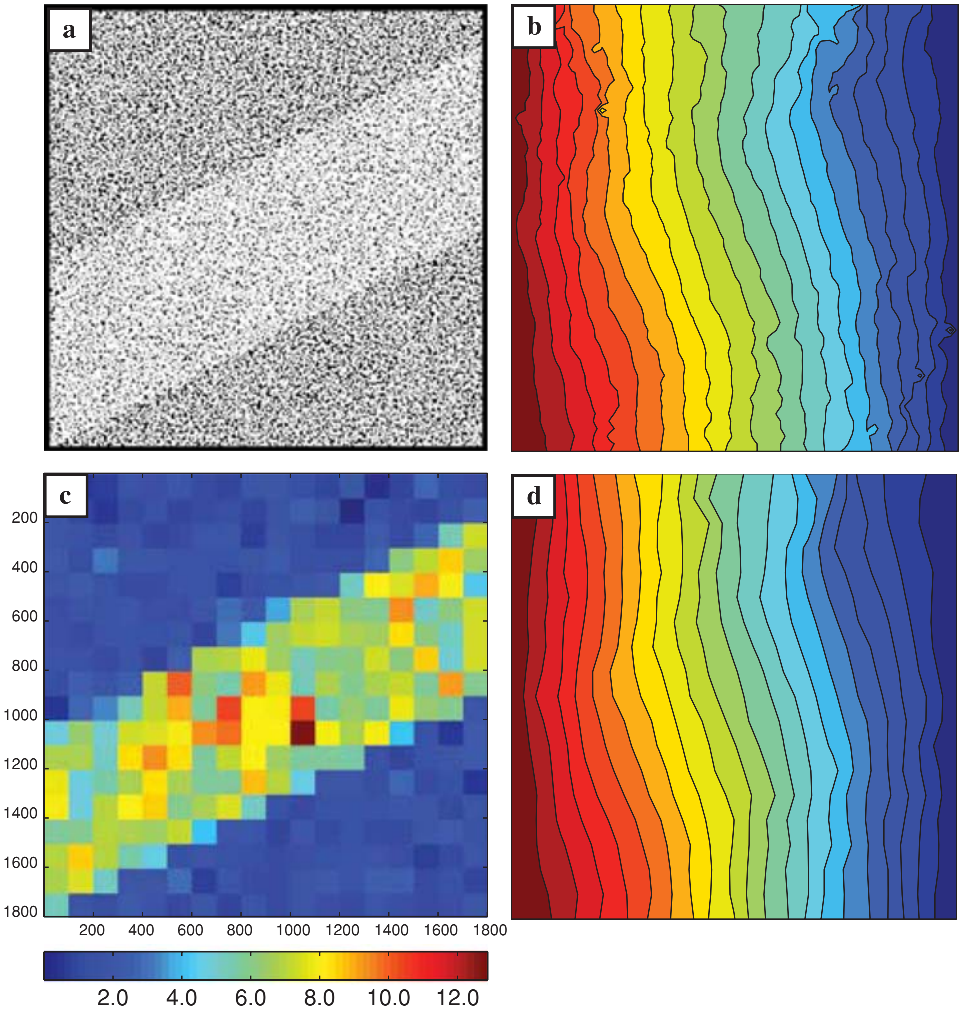

**Fig. 6** **a** Pore/void image for a dilation band analog. **b** Pressure field from reference solution. **c** Permeability field ($k_{11}$) measured by sub-cell LB simulations. **d** Predicted pressure field from combined LB–FE approach

strict comparison of the two times is ambiguous. The LB–FE approach provides a full characterization of the permeability field and allows one to solve additional boundary-value problems with trivial additional computational effort. This is not the case with a simple LB solution. We also note that our LB implementation does not take advantage of several methods available for accelerating convergence, such as the method of Verberg and Ladd [30]. Interestingly, this method has even larger memory requirement than the standard LB algorithm (on the order of 50% extra) so that savings in computational time are balanced by the need for greater memory. Utilizing the framework presented here, however, one might take advantage of both improved convergence and dramatic memory savings.

We conclude this section with a brief refinement study based on the homogeneous example, to illustrate the importance of choosing a proper discretization. Figure 7 illustrates the relative error in the predicted sample permeability for a large range of element sizes. Above an element dimension of 1/18, the REV size we identified using our dissipation methodology, we see that the relative error remains bounded below 2%. The striking feature of this graph, however, is the solution behavior as one chooses extremely small elements. We notice a sharp jump in error, indicating that the elements are no longer sufficiently large to be representative, and are dominated by large microscale fluctuations in element properties.

There is one further observation to be made concerning REVs for anisotropic media. The defining characteristic of anisotropy is the fact that in different directions different percolating pathways are activated, and the primary transport mechanisms may change radically. A typical example would be a medium containing a series of subparallel fractures that may

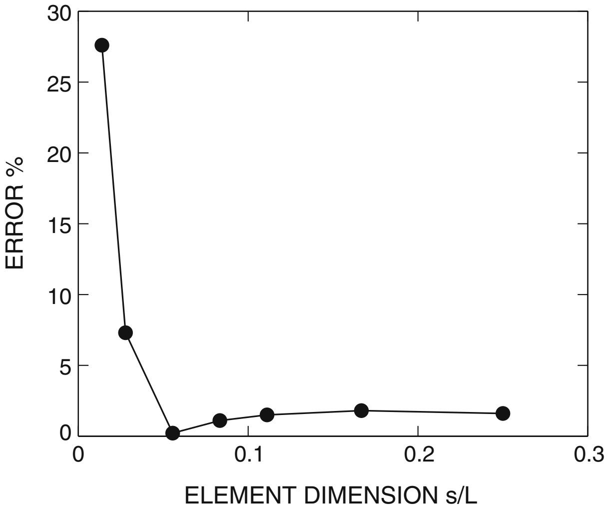

**Fig. 7** Mesh refinement study for the homogeneous example. *Data points* represent relative error in predicted effective permeability, based on the reference LB solution

become active or inactive depending on the local hydraulic gradient. Thus, when dealing with such anisotropy, there is no reason to expect that the REV for a particular flow direction corresponds to the necessary REV for an alternative flow direction. Therefore, care should be taken when determining the necessary element size such that the chosen REV is appropriate for the entire suite of problems to be modeled.

## 4 Castlegate sandstone

To this point, our examples have all been artificially generated. In practice, however, one would most likely be interested in 3D simulations based on actual geologic microstructures. To this end, we conclude our numerical examples with an example based on real data from a natural sandstone sample from the Castlegate Formation (Cretaceous Mesa Verde Group, eastern Utah). This fine- to medium-grained (~0.2 mm grain size) sandstone is commonly used in experimental rock mechanics studies as an analogue reservoir rock. A detailed description of the phase distribution is provided in [11, 12]. Figure 8 presents an image of the solid phase of the sandstone specimen. As reported by Fredrich et al. [14], data for several sandstone samples was originally collected using synchrotron microtomography at the Argonne Advanced Photon Source and passed through a series of post-processing steps to produce the final microtomographic images. A synchrotron provides a high-energy, monochromatic X-ray source that avoids many of the disadvantages of standard X-ray tomography techniques such as beam hardening [14, 24, 25]. As a result, one is able to gather high-resolution, high-quality images. The drawback is that sample sizes are correspondingly small. The image resolution for this Castlegate sample is 3.34 μm, while the overall sample volume is 1.4 mm$^3$.

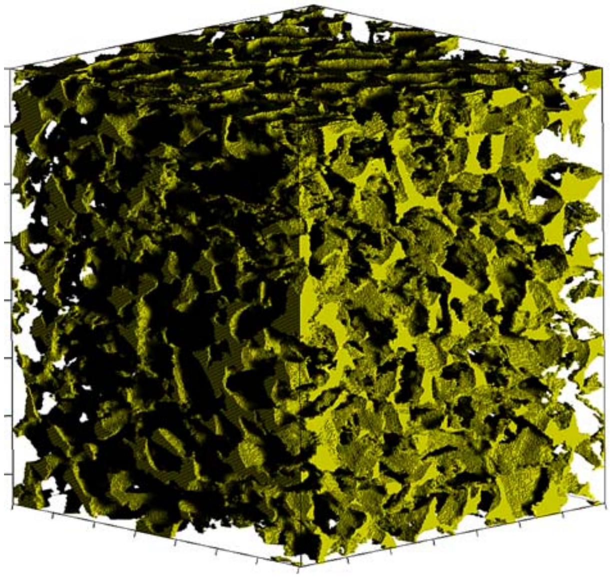

**Fig. 8** Microtomographic image of the solid phase of a Castlegate sandstone. Image resolution is 3.34 μm. Image volume is 1.4 mm$^3$. Image reproduced from [14]

Fredrich et al. then ran detailed LB simulations based on the resulting images. They compared the predicted permeability with laboratory permeametry experiments performed on centimeter-scale cores from the same specimens, finding excellent agreement among all samples. The permeability of Castlegate sandstone has been well-characterized experimentally by several authors, and generally falls in the range 0.8–1.2 μm$^2$. The LB simulations of the Castlegate samples fell in the range 0.8–1.0 μm$^2$. Given the demonstrated ability of the LB method to predict macroscale permeability, we wished to see if we could get similar results using a combined LB–FE approach.

As before, we ran a reference LB simulation in the entire domain of our specimen. Constant pressure conditions were specified on an inlet and outlet face, and normal flow was prevented along the other four boundaries. We interject that these boundary conditions are an arbitrary choice, and one can imagine a variety of other configurations for an upscaling study. Several have been presented in the literature, with advantages and disadvantages to each. Our purpose here is not to advocate a particular choice, but rather compare two methods in which consistent conditions have been applied. Our pressure formulation is detailed in an appendix. The computation was run in parallel on eight processors of a distributed memory cluster, with steady state reached after approximately 26 h (206 h of total wall time). Again, we used the resulting velocity field to calculate the local rate of mechanical dissipation, and averaged it over increasingly large volumes (Fig. 9). From this analysis, we determined that a $3 \times 3 \times 3$ discretization of the domain would yield appropriately sized REVs. Figure 10 illustrates the FE mesh and boundary conditions we have used. We note that oscillations in the dissipation graph are fairly sizeable even as one approaches the global sample size. This is not surprising given the extremely small sample dimensions. Nevertheless, we will see that reasonable results can be achieved despite seemingly large fluctuations.

With the domain thus divided into 27 elements, 81 separate sub-cell simulations were required to determine the 27 local permeability tensors. Table 2 provides the complete tensor for a few typical elements, which display significant asymmetry and anisotropy. Table 3 compares the predicted effective $k_{11}$ permeability of the sandstone sample. Our predicted permeability value of 0.89 $\mu m^2$ is in agreement with both the full LB solution and with the experimental range presented earlier. Again, we have also presented results based on the tensor form: asymmetric, symmetrized, and isotropic. Using the full, asymmetric tensor provides the best solution, with errors increasing as one introduces symmetry and isotropy assumptions. These results suggest that, in practice, the full tensor is most appropriate. We also observe a significant execution speedup and dramatic savings in required memory. It appears then that the LB–FE methodology provides a reasonable method for estimating a macroscale permeability value in a computationally efficient manner.

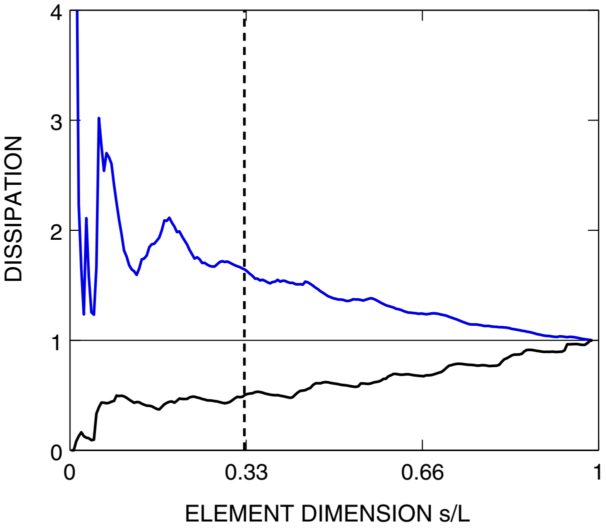

**Fig. 9** Mechanical dissipation rate averaged over increasingly large volumes at two different locations in the domain, normalized with respect to the global average

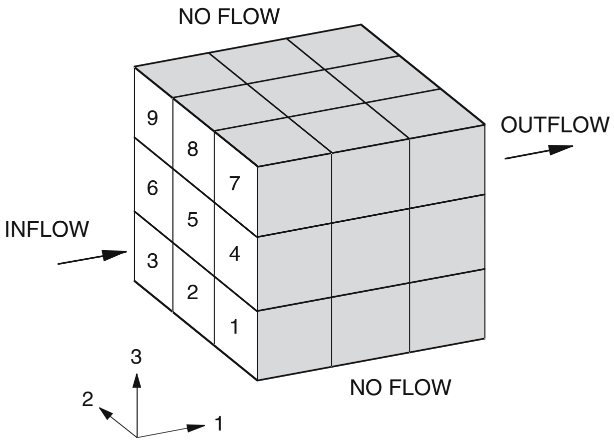

**Fig. 10** $3 \times 3 \times 3$ FE discretization used in the Castlegate example. Normal flow is prevented along shaded boundaries

## 5 Closure

Several key issues have been addressed in this paper. The first and foremost revolves around the notion of the effective permeability as it applies to an REV. The REV is the boundary between the micro-scale and Darcy scale, and as such it represents the smallest volume over which a granular material with a complex microstructure may be considered a continuum. Although the notion of an REV has been accepted in principle, it is challenging to quantify in practice. In this paper we used the local rate of mechanical dissipation to quantify the REV for an actual sandstone, not only for calculating its overall effective permeability but also for describing how this very important material parameter varies spatially throughout the sample. Clearly, the spatial distribution of effective permeability provides much more information than the overall permeability itself, even if the volume of interest is only 1.4 $mm^3$.

None of these ideas would be useful in practice without the recent advances in high resolution 3D imaging and powerful numerical modeling techniques currently at our disposal. High resolution 3D synchrotron-computed microtomography combined with the powerful lattice Boltzmann-finite element hybrid method is an enviable combination to attack the pore scale hydrodynamics problem. The proposed LB–FE

**Table 2** Element permeability components ($\mu m^2$) following the numbering scheme noted in Fig. 10

| Element | $k_{11}$ | $k_{22}$ | $k_{33}$ | $k_{21}$ | $k_{12}$ | $k_{31}$ | $k_{13}$ | $k_{32}$ | $k_{23}$ |
|---|---|---|---|---|---|---|---|---|---|
| 1 | 2.4e-1 | 2.0e-1 | 1.5e-1 | –2.3e-2 | –6.6e-3 | 3.7e-2 | 3.5e-2 | –3.5e-2 | 1.5e-1 |
| 2 | 2.6e-1 | 5.1e-1 | 3.3e-1 | –6.9e-3 | 4.2e-2 | –1.0e-2 | –7.4e-2 | –7.9e-3 | 3.3e-1 |
| 3 | 8.4e-1 | 5.1e-1 | 5.4e-1 | –4.3e-1 | –1.7e-1 | 2.8e-1 | –6.4e-2 | –4.0e-2 | 5.4e-1 |
| 4 | 9.6e-1 | 1.7 | 5.4e-1 | –1.8e-1 | –3.0e-1 | 2.1e-2 | –3.2e-2 | 2.7e-1 | 5.4e-1 |
| 5 | 1.2 | 6.2e-1 | 7.1e-1 | –2.6e-2 | 4.0e-2 | 2.6e-1 | 3.6e-2 | 9.2e-2 | 7.1e-1 |
| 27 | 1.1 | 9.0e-1 | 9.5e-1 | –2.6e-1 | –1.1e-1 | –5.0e-2 | –3.7e-2 | 6.1e-2 | 1.3e-1 |
| Average | 1.2 | 8.3e-1 | 7.9e-1 | –5.7e-4 | –2.1e-2 | 4.2e-2 | 1.9e-3 | 4.8e-3 | –3.5e-2 |

We have not listed all 27 elements for brevity

**Table 3** Castlegate effective $k_{11}$ permeability values from both the reference solution and the LB–FE approach

| Method | $\mu m^2$ | Error (%) | Hours | Memory (Mb) |
|---|---|---|---|---|
| Reference solution | 0.893 | | 206.1 | 1,630 |
| Full tensor | 0.911 | 2.0 | 30.8 | 60 |
| Symmetrized | 0.845 | 5.4 | 30.8 | 60 |
| Isotropic | 0.803 | 10.1 | 30.8 | 60 |

All simulations were run on identical 3.06 GHz processors

technique has dual advantages in that it not only quantifies the spatial variation of effective permeability, it also reduces the computing time and memory requirements. Hybrid techniques are by no means unique, but to the knowledge of the authors this is the first time that the combined LB–FE methods have been used for pore scale hydrodynamics on very high-resolution images. As an aside, we noted that the full (asymmetric) effective permeability tensor enhances the accuracy of the LB–FE approach particularly in 3D simulations. Other challenges ahead include enhancing the performance of the LB–FE technique and developing more robust computational platforms for upscaling the modeling further to field dimensions.

**Acknowledgments** The first author gratefully acknowledges the support of a Stanford Graduate Fellowship, a National Science Foundation Graduate Research Fellowship, and two summer Graduate Research Internships at Sandia National Laboratories. The second author acknowledges the support of the U.S. Department of Energy Grant DE-FG02-03ER15454, and the U.S. National Science Foundation, Grant CMS-0324674. The first and third author acknowledge support from the U.S. Department of Energy, Office of Basic Energy Sciences, Chemical Sciences and Geosciences Program. Portions of this work were performed at Sandia National Laboratories funded by the US DOE under Contract DE-AC04-94AL85000. Sandia is a multiprogram laboratory operated by Sandia Corporation, a Lockheed Martin Company, for the United States Department of Energy's National Nuclear Security Administration. We are grateful to David Noble of Sandia National Laboratories for helpful discussions concerning boundary conditions, and to Professor Atilla Aydin of Stanford University for allowing the reproduction of Fig. 4. We are also grateful to two anonymous reviewers for their constructive comments. Much of the computation was performed on Sandia's 256-node ICC Liberty cluster.

## Appendix: Pressure boundary condition

In the LB method, pressure and density are related through the equation of state

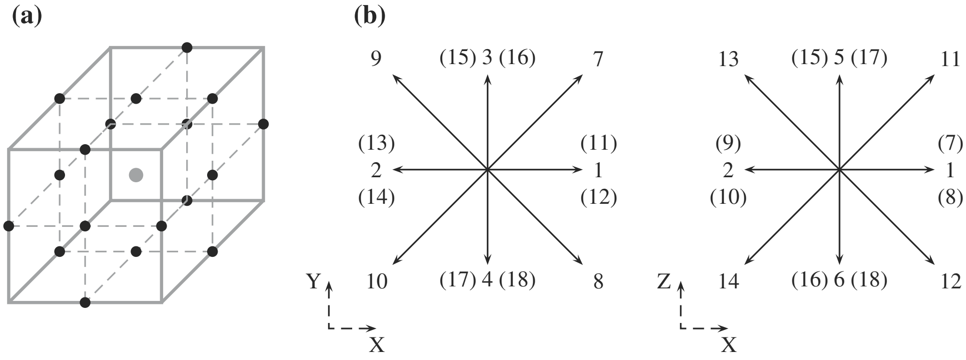

**Fig. 11** **a** Typical unit cell for a D3Q19 lattice. Rest node is *gray*, and 18 neighbor nodes are *black*. Link vectors are omitted for clarity. **b** Two orthogonal views of the D3Q19 lattice, illustrating the present numbering scheme. Out-of-plane links are noted with parentheses

$$p = c^2\rho, \tag{4}$$

where $c$ is the speed of sound (for a perfect gas) on the given lattice. To impose a pressure boundary condition, we therefore seek to impose a specified density. Recall that the density $\rho$ and macroscopic flow velocity $\boldsymbol{u}$ are defined in terms of the discrete particle distributions $f_i$ and their associated velocities $\boldsymbol{e}_i$,

$$\rho = \sum_{i=0}^{18} f_i; \quad \rho\boldsymbol{u} = \sum_{i=1}^{18} f_i\boldsymbol{e}_i. \tag{5}$$

In our 3D simulations, we have used a D3Q19 lattice consisting of 18 neighbor links and one rest state. Figure 11 illustrates the basic lattice unit and the numbering scheme we have employed.

Consider a typical lattice node located on the inlet boundary. At this node we assign a density $\rho_{\text{in}}$, and further specify $u_y = u_z = 0$. Consider now the density distribution after the streaming step in a typical LB iteration. Any particle population coming from an interior node becomes a known quantity. On the other hand, $f_1$, $f_7$, $f_8$, $f_{11}$, and $f_{12}$ remain undetermined since these populations stream from points outside the domain. We therefore seek to determine these five unknowns such that they satisfy the specified density and velocity conditions.

To shorten notation let us group the particle populations into three sets according to whether $e_x = 1, 0,$ or –1.

$$X^+ = \{1, 7, 8, 11, 12\}. \tag{6}$$

$$X^o = \{0, 3, 4, 5, 6, 15, 16, 17, 18\}. \tag{7}$$

$$X^- = \{2, 9, 10, 13, 14\}. \tag{8}$$

In this notation, any $f_i \in X^+$ is an unknown. Our first task is to determine the inlet velocity $u_x$ in terms of the known populations. From the density and momentum equations

$$\rho_{\text{in}} = \sum_{X^-} f_i + \sum_{X^o} f_i + \sum_{X^+} f_i, \tag{9}$$

$$\rho_{\text{in}} u_x = \sum_{X^+} f_i - \sum_{X^-} f_i, \tag{10}$$

which implies

$$u_x = 1 - \frac{1}{\rho_{\text{in}}}\left[\sum_{X^o} f_i + 2\sum_{X^-} f_i\right]. \tag{11}$$

Now that the complete vector $\boldsymbol{u}$ is determined, our goal is to find a particle distribution that satisfies Eqs. 5. These relations, however, are insufficient to determine the unknown $f_i$ uniquely. In light of this fact, we have adopted an approach like that of Zou and He [32]. We note that the equilibrium particle distribution also satisfies the momentum equations,

$$\sum_{i=1}^{18} f_i^{\text{eq}}\boldsymbol{e}_i = \rho\boldsymbol{u}. \tag{12}$$

This implies that the unknown $f_i$ must satisfy the following in order to maintain the appropriate $x$-momentum:

$$\sum_{X^+} f_i - \sum_{X^-} f_i = \sum_{X^+} f_i^{\text{eq}} - \sum_{X^-} f_i^{\text{eq}}. \tag{13}$$

Let us denote by $\bar{f}_i$ the particle population traveling in the opposite direction to $f_i$; that is, $\boldsymbol{e}_i$ and $\bar{\boldsymbol{e}}_i$ point in opposite directions. Zou and He noted that by choosing the unknown $f_i$ such that

$$f_i - f_i^{\text{eq}} = \bar{f}_i - \bar{f}_i^{\text{eq}}, \tag{14}$$

Eq. 13 is automatically satisfied. They described this approach as a “bounceback rule“ for the non-equilibrium distribution, in analogy to the commonly used bounceback rule for dealing with solid interfaces. In the D3Q19 model, the equilibrium distributions are given by

$$f_i^{\text{eq}} = \rho\omega_i\left[1 + 3\boldsymbol{u}\cdot\boldsymbol{e}_i + \frac{9}{2}(\boldsymbol{u}\cdot\boldsymbol{e}_i)^2 - \frac{3}{2}\boldsymbol{u}\cdot\boldsymbol{u}\right], \tag{15}$$

with weights $\omega_i$ = 1/3, 1/18, and 1/36 for the rest particle, nearest neighbor links, and diagonal links, respectively.

With this simple heuristic in hand, a scheme emerges for determining the unknown particle populations. First, we fix the unknown component normal to the inlet plane,

$$f_1 = f_2 + \left(f_1^{\text{eq}} - f_2^{\text{eq}}\right) = f_2 + \frac{1}{3}\rho_{\text{in}} u_x. \tag{16}$$

For the four remaining unknowns, we apply a similar bounceback rule to ensure that the $x$-momentum equation is satisfied. We also note, however, that we can adjust the $y$ and $z$-momenta without altering the $x$-momentum by using the populations tangential to the inlet plane, $f_i \in X^o$. In particular, we choose

$$f_7 = f_{10} + \frac{1}{2}(f_4 + f_{17} + f_{18}) - \frac{1}{2}(f_3 + f_{15} + f_{16}) + \frac{1}{6}\rho_{\text{in}} u_x, \tag{17}$$

$$f_8 = f_9 - \frac{1}{2}(f_4 + f_{17} + f_{18}) + \frac{1}{2}(f_3 + f_{15} + f_{16}) + \frac{1}{6}\rho_{\mathrm{in}} u_x, \tag{18}$$

$$f_{11} = f_{14} + \frac{1}{2}(f_6 + f_{16} + f_{18}) - \frac{1}{2}(f_5 + f_{15} + f_{17}) + \frac{1}{6}\rho_{\mathrm{in}} u_x, \tag{19}$$

$$f_{12} = f_{13} - \frac{1}{2}(f_6 + f_{16} + f_{18}) + \frac{1}{2}(f_5 + f_{15} + f_{17}) + \frac{1}{6}\rho_{\mathrm{in}} u_x. \tag{20}$$

These algebraic expressions determine the unknown $f_i$ such that $\rho = \rho_{\mathrm{in}}$ and $u_y = u_z = 0$. An identical approach is applied to outlet nodes, except the unknowns become $f_i \in X^-$.

$$u_x = \frac{1}{\rho_{\mathrm{out}}}\left[\sum_{X^o} f_i + 2\sum_{X^-} f_i\right] - 1. \tag{21}$$

$$f_2 = f_1 - \frac{1}{3}\rho_{\mathrm{out}} u_x. \tag{22}$$

$$f_9 = f_8 + \frac{1}{2}(f_4 + f_{17} + f_{18}) - \frac{1}{2}(f_3 + f_{15} + f_{16}) - \frac{1}{6}\rho_{\mathrm{out}} u_x. \tag{23}$$

$$f_{10} = f_7 - \frac{1}{2}(f_4 + f_{17} + f_{18}) + \frac{1}{2}(f_3 + f_{15} + f_{16}) - \frac{1}{6}\rho_{\mathrm{out}} u_x. \tag{24}$$

$$f_{13} = f_{12} + \frac{1}{2}(f_6 + f_{16} + f_{18}) - \frac{1}{2}(f_5 + f_{15} + f_{17}) - \frac{1}{6}\rho_{\mathrm{out}} u_x. \tag{25}$$

$$f_{14} = f_{11} - \frac{1}{2}(f_6 + f_{16} + f_{18}) + \frac{1}{2}(f_5 + f_{15} + f_{17}) - \frac{1}{6}\rho_{\mathrm{out}} u_x. \tag{26}$$

## References

1. Andrade JE, Borja RI (2006) Quantifying sensitivity of local site response models to statistical variation in soil properties. Acta Geotechnica 1:3–14
2. Arns CH, Knackstedt MA, Val Pinczewski W, Martys NS (2004) Virtual permeametry on microtomographic images. J Pet Sci Eng 45:41–46
3. Aydin A, Borja RI, Eichhubl P (2006) Geological and mathematical framework for failure modes in granular rock. J Struct Geol 16:941–959
4. Baxevanis T, Papamichos E, Flornes O, Larsen I (2006) Compaction bands and induced permeability reduction in Tuffeau de Maastricht calcarenite. Acta Geotechnica 1:123–135
5. Bear J (1972) Dynamics of fluids in porous media. American Elsevier, New York
6. Bhatnagar P, Gross E, Krook M (1954) A model for collision processes in gases. I. Small amplitude processes in charged and neutral one-component systems. Phys Rev E 94:511
7. Borja RI (2006) Conditions for instabilities in collapsible solids including volume implosion and compaction banding. Acta Geotechnica 1:107–122
8. Borja RI (2006) HEAT, a 3D finite element heat conduction program. Stanford University, Stanford
9. Borja RI, Aydin A (2004) Computational modeling of deformation bands in granular media. I. Geological and mathematical framework. Comput Methods Appl Mech Eng 193:2667–2698
10. Chen S, Doolen GD (1998) Lattice Boltzmann method for fluid flows. Annu Rev Fluid Mech 30:329–364
11. DiGiovanni AA, Fredrich JT (2006) Micromechanics of compaction in an analogue reservoir sandstone. In: Couples G, Meredith P, Main I (eds) Fracture, damage and related deformation features. Special Publication Geological Society (in press)
12. DiGiovanni AA, Fredrich JT, Holcomb DJ, Olsson WA (2000) Micromechanics of compaction in an analogue reservoir sandstone. In: Proceedings of the 4th U.S. Rock Mech. Symposium, pp 1153–1160
13. Ferreol B, Rothman DH (1995) Lattice-Boltzmann simulations of flow through Fontainebleau sandstone. Transp Porous Media 20:3–20
14. Fredrich JT, DiGiovanni AA, Noble DR (2006) Predicting macroscopic transport properties using microscopic image data. J Geophys Res 111:B03201
15. Fredrich JT, Menendez B, Wong TF (1995) Imaging the pore structure of geomaterials. Science 28:276–279
16. Keehm Y, Mukerji T, Nur A (2004) Permeability prediction from thin sections: 3D reconstruction and lattice-Boltzmann flow simulation. Geophys Res Lett 31:L04606
17. Maier RS, Bernard RS, Grunau DW (1996) Boundary conditions for the lattice Boltzmann method. Phys Fluids 8:1788–1801
18. Manwart C, Aaltosalmi U, Koponen A, Hilfer R, Timonen J (2002) lattice-Boltzmann and finite-difference simulations of the permeability for three-dimensional porous media. Phys Rev E 66:016702
19. Martys N, Chen H (1996) Simulation of multicomponent fluids in complex three-dimensional geometries by the lattice Boltzmann method. Phys Rev E 53:743–750
20. Noble DR, Chen S, Georgiadis JG, Buckius RO (1995) A consistent hydrodynamic boundary condition for the lattice Boltzmann method. Phys Fluids 7:203–209
21. O'Connor RM, Fredrich JT (1999) Microscale flow modeling in geologic materials. Phys Chem Earth (A) 24:611–616
22. Pilotti M, Succi S, Menduni G (2002) Energy dissipation and permeability in porous media. Europhys Lett 60:72–78
23. Qian Y, d'Humieres D, Lallemand P (1992) Lattice BGK models for the Navier–Stokes equation. Europhys Lett 17:479
24. Sham TK, Rivers ML (2002) A brief overview of synchrotron radiation. In: Fenter PA (ed) Applications of synchrotron radiation in low-temperature geochemistry and environmental science. Reviews in Mineralogy and Geochemistry, vol 49, Mineralogical Society of America, Washington DC, pp 117–147
25. Spanne P, Thovert JF, Jacquin CJ, Lindquist WB, Jones KW, Adler PM (1994) Synchrotron computed microtomography of porous media: Topology and transports. Phys Rev Lett 73:2001–2004

26. Sternlof KR, Chapin JR, Pollard DD, Durlofsky LJ (2004) Permeability effects of deformation band arrays in sandstone. AAPG Bull 88:1315–1329
27. Sternlof KR, Karimi-Fard M, Pollard DD, Durlofsky LJ (2006) Flow and transport effects of compaction bands in sandstones at scales relevant to aquifer and reservoir management. Water Resour Res 42:W07425
28. Succi S (2001) The lattice Boltzmann equation for fluid dynamics and beyond. Oxford University Press, Oxford
29. Ulm F-J, Abousleiman Y (2006) The nanogranular nature of shale. Acta Geotechnica 1:77–88
30. Verberg R, Ladd AJC (1999) Simulation of low-Reynolds-number flow via a time-independent lattice-Boltzmann method. Phys Rev E 60:3336–3373
31. Zhu W, Wong T-F (1997) The transition from brittle faulting to cataclastic flow: permeability evolution. J Geophys Res 102:3027–3041
32. Zou Q, He X (1997) On pressure and velocity boundary conditions for the lattice Boltzmann BGK model. Phys Fluids 9:1591–1598